Advanced analysis of the bias-extension of woven fabrics with X-ray microtomography and Digital Volume Correlation

O. Stamati [a], L. Orgéas [a,*], S. Rolland du Roscoat [a], P. Lhuissier [b], P.J.J. Dumont [c], F. Martoïa [c]

[a] *Univ. Grenoble Alpes, CNRS, Grenoble INP, 3SR Lab, F-38000 Grenoble, France*
[b] *Univ. Grenoble Alpes, CNRS, Grenoble INP, SIMAP, F-38000 Grenoble, France*
[c] *Univ. Lyon, INSA-Lyon, CNRS, LaMCoS, UMR5259, 69621 Villeurbanne, France*

ARTICLE INFO

ABSTRACT

The bias-extension test is widely used to study the mechanics of woven fabrics undergoing large deformation. Standard analyses focus on the in-plane shear deformation, but rarely on other deformation modes. Here, the bias-extension of a basalt fiber twill was performed inside a X-ray microtomograph to get 3D *in situ* observations. The 3D images were used in a dedicated Digital Volume Correlation procedure that enabled relevant 3D strain invariants to be estimated. Coupled with important in-plane shear and moderate tension along the yarns, significant 3D compaction was observed as a complex combination involving out-of-plane auxetic expansion and in-plane compaction. The transition between sheared regions extends to 2–3 unit cells of the fabric, highlighting the role of the fibrous micro and mesostructures. This unique 3D experimental database enriches the knowledge on the mechanics of woven fabrics and provides valuable information for the development of generalized continuum approaches to model their mechanical behavior.

1. Introduction

Thanks to both their good specific mechanical properties and deformability, woven fabrics are widely used in fiber-reinforced composites and have attracted increasing attention for a wide field of applications, including aeronautics, automotive, civil infrastructure, sport. The manufacturing processes of woven fabric-reinforced composites often involve a forming stage during which woven fabrics are deformed so as to confer them the desired shape of the composite parts. During this stage, woven fabrics usually exhibit severe deformations altering the properties of the composite parts. Consequently, characterizing, understanding and modeling the deformation of woven fabrics has been the subject of numerous studies. A large number of these studies mainly focus on the in-plane shear of woven fabrics, which is known to be their principal deformation mode during their forming stages [1–4]. Bias-extension tests are usually employed purposely [2,5,6]. These tests consist in stretching slender rectangular woven fabric samples of gauge length L with warp and weft directions orientated symmetrically with respect to the loading axis. Upon loading at a stretch displacement d, four different zones (A, B, C, D, see Fig. 1) along the half length of the samples arise, as the shear angles γ between the weft and the warp increase. The well-known first order geometrical analysis of the test, that considers rigid yarns, no slippage and no steric hindrance at yarn-yarn contact points as basis assumptions [5], yields to an expression of the shear angle:

$$\gamma = \frac{\pi}{2} - 2\arccos\left(\frac{L+d}{\sqrt{2}L}\right) \tag{1}$$

which, according to this simplified theory, is spatially homogeneous in the central zone D of the sample, whereas this angle is equal to 0 and $\gamma/2$ in the zone A below the clamps, and in zones B and C, respectively.

Nevertheless, the strong multiscale nature of textiles, with length-scales ranging from the microscale (or the fiber scale) with highly flexible and non-cohesive filaments, the mesoscale (or the fiber yarn scale) up to the macroscale (or the part scale) results in 3D highly anisotropic architectures with complex 3D and multi-scale deformation modes. An important set of experimental evidences demonstrated that these architectures strongly alter the macroscopic mechanical behavior of woven fabrics, specifically during bias-extension, thus questioning the relevance of the aforementioned geometrical approach and, in particular, Eq. (1). For example, complex macroscale phenomena with shear strain localization with finite band-width rather than abrupt changes have been observed during bias-extension tests [2,4,7]. These macroscale deformation mechanisms are strongly linked with the mesoscale ones such as the bending, twisting, shear and compaction of yarns [8], which are in turn coupled with microscale ones such as fiber rearrangement, bending and twisting [9].

---

* Corresponding author.
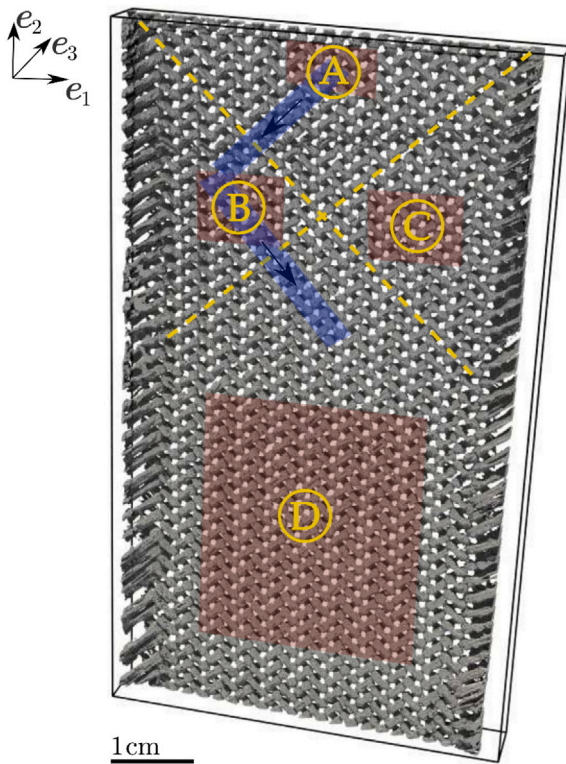*E-mail address:* laurent.orgeas@3sr-grenoble.fr (L. Orgéas).

Fig. 1. 3D half-view of the twill-fabric (at the reference state) used for bias-extension. The characteristic regions A, B, C and D of theoretical constant shear strain are depicted. The red shadowed areas represent zones over which the measured strain fields were averaged, while the blue ones represent zones along with the strain paths were followed, *i.e.*, between the adjacent regions A–B (from A to B, see the arrow) and B–D (from B to D, see the arrow).

To accurately describe this complex behavior in macroscale constitutive theories (and thus to properly model the forming processes of woven fabric-reinforced composites), not only the in-plane shear but also other deformation mechanisms should be characterized and taken into account such as the weft and warp elongation, the volume and in-plane surface variations. These mechanisms are often neglected in most first order continuum approaches, except in some studies that tried to incorporate them using physically-based strain invariants [8,10]. In addition, the inability of first order approaches to properly model the aforementioned strain localization phenomena [4] yielded some authors to propose recently enriched continuum models [11–13] or similar alternatives [14,15], which offer more realistic descriptions, but which still lack experimental data to be well-cast, in particular for deformation modes other than in-plane shear.

Thus, there is a need for new experimental data. For that purpose, non-destructive testing techniques offer new possibilities. Acoustic emission [16,17], optical microscopy [18], electron microscopy [19], infrared thermography [20], are some examples applied to textile composites. Among them, the Digital Image Correlation (DIC) technique [21], which gives access to displacement and strain fields on the surface of the material, has gained significant interest in the field of textile testing [2,22–25]. The last studies highlighted the importance of using local displacement and strain measurements providing interesting guidelines to understand the large deformation mechanics of fibrous fabrics used in composites.

However, DIC is only limited to surface measurements, which is often insufficient to completely characterize the 3D anisotropic mechanical response of textiles. On the contrary, X-ray tomography is extremely well-suited since it permits the visualization of the internal 3D structure of materials [26,27]. For instance, 3D X-ray images

of fibrous reinforcements used in composites can be used either to generate numerical meso-models and to perform qualitative comparisons between images and simulations [8,28] or to estimate other properties such as permeability [29,30]. Beyond the visualization and the quantification of the internal structure via 3D image analysis, X-ray tomography provides the ability to conduct *in situ* mechanical tests. Studies employing *in situ* X-ray experiments have been notably performed to analyze the mechanical behavior and the damage of fiber-reinforced composites [31–34], but also their structural evolution during their forming processes [9,29,35,36]. The insights brought by these experiments are numerous and relevant and can be further enhanced when image analysis is enriched to extract local displacement fields either by using 3D semi-discrete correlation [37] or Digital Volume Correlation (DVC), *i.e.*, the extension of DIC to 3D images [32, 38,39].

However, to the best of the authors knowledge, there is no study in the literature that aimed at analyzing the 3D mechanics of fibrous woven fabrics subjected to finite strains loadings (*e.g.* via bias-extension), by combining simultaneously 3D *in situ* observations (*e.g.* with X-ray microtomography) and the measurements of the related 3D kinematic fields (*e.g.* with DVC). This results in a lack of 3D experimental data to understand and to model the complex mechanics of fibrous architectures. One difficulty to overcome to achieve such an investigation is to properly carry out DVC analyses with thin and quasi-periodic materials (such as the standard 2D woven fabrics used in composites) subjected to finite geometrical transformations similar to those encountered by these woven fabrics during their forming. Within this context, we propose a method that allows to provide novel experimental data regarding the 3D quantitative description of the macroscale mechanics occurring in a dry basalt woven fabric subjected to finite strains and rotations during bias-extension. The aim is to address crucial but still open questions regarding the role of the fabric out-of-plane deformation, 3D compaction, in-plane bending, but also the coupling of these deformation modes with the dominant in-plane shear. Such an experimental quantitative description is expected to provide useful information to improve and justify theoretical assumptions of constitutive models developed for the mechanics of fabrics, as well as to validate their prediction to optimize the forming processes of woven-fabric-reinforced composites.

2. Material and methods

2.1. Material

A balanced twill fabric (2×2), with an areal density of 600 g m^{-2}, a thickness of 0.7 mm $\pm$ 0.035 mm (which was estimated according to the method reported in Section 3.1) and with weft and warp made of identical basalt fiber bundles (diameter of elementary basalt filaments of 11 μm and linear density of fiber bundles of 550 tex), was used for the experiments. The twill exhibits three material directions, *i.e.*, the weft, the warp and the out-of-plane directions respectively noted $\mathbf{e}_I^0$ (resp. $\mathbf{e}_I$), $\mathbf{e}_{II}^0$ (resp. $\mathbf{e}_{II}$), and $\mathbf{e}_{III}^0$ (resp. $\mathbf{e}_{III}$) in the reference (resp. deformed) configurations. The fabric was purchased from Isomatex (Gembloux, Belgium). On the left-hand side, Fig. 2 shows a macroscale upper view (perpendicular to $\mathbf{e}_{III}^0 = \mathbf{e}_3$) of the twill fabric in the reference plane ($\mathbf{e}_1, \mathbf{e}_2$). The grey level slices reported on the right hand side of the figure have been obtained with X-ray microtomography with a 7^3 μm^3 voxel size. This figure illustrates the complex multiscale and quasi-periodic architecture of the studied woven fabric. The top image is a zoom in the ($\mathbf{e}_1, \mathbf{e}_2$) plane, the middle one is a zoom in the ($\mathbf{e}_1, \mathbf{e}_3$) plane. The bottom image is also a zoom in the ($\mathbf{e}_I^0, \mathbf{e}_3$) plane: the periodic and anisotropic pattern of the twill fabric is highlighted, with a spatial periodicity λ close to 6.3 mm, a yarn height and width measuring 0.35 mm and 1.5 mm, respectively.
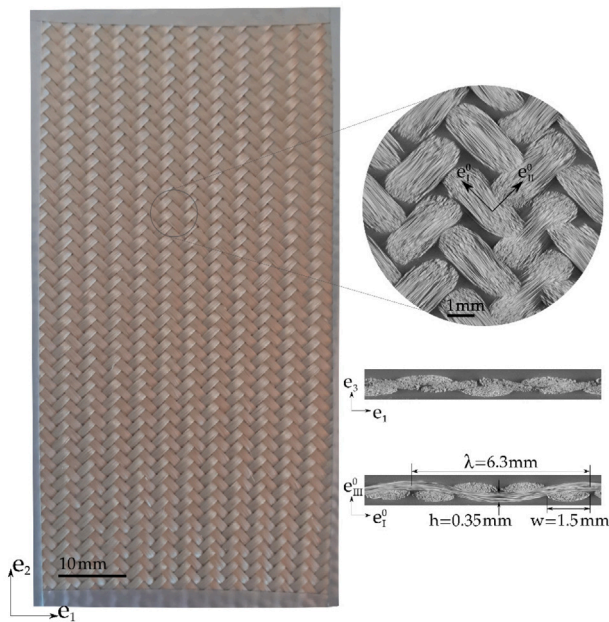
Fig. 2. Left: Upper view photograph of the studied basalt twill fabric. Right: zooms (grey level slices obtained with X-ray tomography) of the structure of the twill: the upper, middle and lower slices have been obtained in the $(\mathbf{e}_1,\mathbf{e}_2)$, $(\mathbf{e}_1,\mathbf{e}_3)$ and $(\mathbf{e}_I^0,\mathbf{e}_3)$ planes, respectively. The bottom slice shows the main characteristics of the periodic architecture of the twill fabric.

Fig. 3. Experimental set-up designed for the *in situ* bias-extension of the basalt twill samples inside the X-ray facility of 3SR Lab.

2.2. Bias-extension test for 3D in-situ observations

The most frequently employed test to characterize the in-plane shear behavior of woven textiles is the bias-extension test [2,5,6]. The test consists in stretching a rectangular woven fabric sample such that its warp $\mathbf{e}_I^0$ and weft $\mathbf{e}_{II}^0$ directions are initially and symmetrically oriented at 45° with respect to the loading direction $\mathbf{e}_2$. The standard elementary geometrical analysis of this test is based on two main assumptions which yield a pantograph of kinematics at the unit cell scale: (i) rigidity of yarns, (ii) rotation of the yarns at their contact points without slippage. The sample stretching thus results in variations of the angles between the warp and weft which, under the aforementioned assumptions, lead to the creation of four different deformation zones along the half length of the samples (see Fig. 1): A, B, (symmetrically) C, and D. Inside each of these regions, the shear angles between the weft and warp are considered as constant. When the ratio between the initial length over the width of the specimen is bigger than two, the weft and warp yarns in the central zone D, in zones B and C, and in zone A are subjected to an in-plane shear deformation of γ, $\gamma/2$ and 0, respectively.

Based on the tensile system used in [35], we designed a new setup to conduct an *in situ* bias-extension test inside a laboratory X-ray tomograph (3SR Lab, Grenoble, France), as illustrated in Fig. 3. Briefly, a pair of clamps were used to grip the samples with in-plane gauge dimensions 50×160 mm² (*i.e.*, with ≈ 22 fiber bundles along the sample width for the weft and the warp). The sample areas clamped by the grips were covered by paperboard in order to avoid any sample slippage in the grips: preliminary tests conducted outside the tomograph showed that there was no slippage with this procedure. Two polypropylene rods with a 16 mm diameter and with low X-ray absorption were used to support the upper clamp, as well as the tensile force during the experiments. The tensile force was measured with a load cell (HBM C9-500 N, load capacity 500 N) which was fastened between the bottom clamp and the ram axis. The steel cylindrical ram axis of 25 mm diameter was fixed to the top of the loading system which was in turn fixed to the rotation stage of the tomograph. The
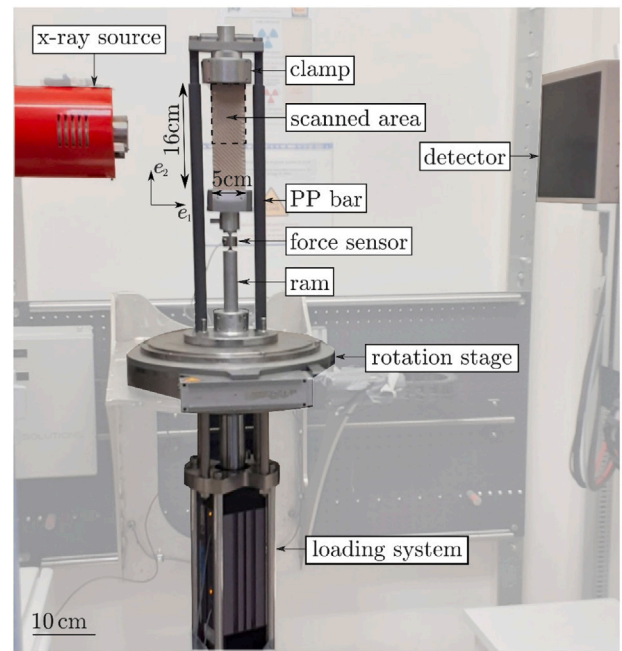
loading system had a maximum load capacity of 15 kN, enabling a ram-speed ranging from 0.1 to 100 µm min⁻¹ and a maximum vertical displacement of 100 mm which was adequate to reach the failure of the tested samples usually occurring around 70 mm, corresponding to a macroscopic averaged elongation of ≈ 1.43.

2.3. Testing procedure

During the mounting of the specimen into the gripping system, particular attention was paid to its alignment along the tensile axis and to preserve its straight shape. For that purpose, before starting the test, the sample was subjected to a very small tensile load that did not alter the initial orthogonal in-plane relative orientation of the weft and the warp. After the relaxation (about 5 min), the first tomographic scan was performed, called hereafter the *reference scan*. Then, the ram was moved down to a first loading step of 10 mm at a constant velocity of 0.25 mm s⁻¹, which corresponds to a mean axial natural strain (or Hencky strain) increment $\Delta\bar{\varepsilon} = \ln((L+d)/L) = 0.06$. A relaxation of 20 min was then performed to stabilize the force and the sample structure. Then a second scan was launched. This sequence was repeated until the last scan, *i.e.*, the scan taken right after the failure of the specimen.

As (i) the studied textile is balanced, (ii) the weft and the warp are symmetrically positioned with respect to the loading axis and thanks to the symmetry of boundary conditions, the sample deformation is symmetrical along the specimen's axis. Thus, to reduce the scanning time, only the upper half of the sample was imaged (as shown in Fig. 3). For that purpose, the voltage and current of the X-ray source were set to 80 kV and 320 µA, respectively, while no extra filter was used. The source operated in a medium spot size mode and the specimen was positioned the closest possible to the source, with the geometrical zoom yielding a voxel size of 30^3 µm³. Note that at this voxel size, individual fibers could not be clearly identified in the reconstructed image. A vertical stack of 3 scans was required to image the entire upper half area of the sample. For each scan, projections were acquired at 2400 different angular positions between 0° and 360°, as the specimen was continuously rotated around a vertical axis. This high number of

projections was selected to compensate for the non-homogeneous X-ray attenuation around the sample (*i.e.*, photons transmitted through the polypropylene rods). In order to reduce the noise level, six images were averaged for each rotation angle. The total duration for each stack of 3 scans was 2 h 45 min.

3. Image analysis

3.1. Binarisation, thickness map, and fiber orientation

For each X-ray scan, a reconstructed 3D greyscale image was obtained by assembling the 2D radiographs using a filtered back projection algorithm, which is available in XAct software (RX-Solutions, Annecy, France). Since fibers attenuate more X-rays compared to air, a standard thresholding operation achieved with the open source Fiji [40] was sufficient to extract the fiber phase from the surrounding air. A 3D view of the extracted textile (*i.e.*, binary image) at the reference state is illustrated in Fig. 1. The characteristic regions A, B, C and D defined previously are also depicted. For each region, we have also sketched (i) the areas over which the measured strain fields (see Section 4.2.2) were averaged, along with (ii) the followed strain paths between the adjacent regions A–B and B–D (see Section 4.2.3).

From the time-series 3D binary images, we assessed the evolution of the sample's thickness together with an estimation of the out-of-plane natural (or Hencky) strain $\varepsilon_{III} = \ln(h/h_0)$ along the out-of-plane direction $\mathbf{e}_{III}$. This first order estimation was used as a complementary/validating information of the out-of-plane deformation, as measured by DVC (see Section 3.2). For this, a 3D grid was defined in each binary image, the geometry of which displayed one mesh along $\mathbf{e}_{III}$ and is identical to the correlation grid used for DVC (discussed in Section 3.2 and shown in Fig. 4d). For each mesh and each of its in-plane pixel, we measured the distance between the first and the last voxels of the thresholded twill along $\mathbf{e}_{III}$, the average of these distances in the considered mesh corresponding to the mean twill height h in it. As an illustration, the measured thickness map of the textile in the reference configuration has been reported in Fig. A.10.

In addition, the projections of the 3D greyscale images in the twill mid-plane ($\mathbf{e}_I$, $\mathbf{e}_{II}$) resulted in 2D enhanced radiographs of the textile sample (see for example Fig. 5). Combined with the plugin OrientationJ [41] of ImageJ, which is based on the evaluation of the gradient structure tensors, these projections were used to estimate the shear angle $\gamma = \pi/2 - \widehat{(\mathbf{e}_I, \mathbf{e}_{II})}$ in the central zone D, as a complementary/validating information of the DVC measurements.

3.2. Digital Volume Correlation (DVC)

To measure the macroscale 3D kinematic fields during the *in situ* bias-extension test, we used the local version of the Digital Volume Correlation (DVC) technique [42,43]. It must be highlighted here that the application of DVC to analyze the mechanical behavior of the considered woven fabric under the considered loading is not straightforward. The challenging issues to overcome are induced by (i) the quasi-periodic architectures of woven fabrics combined with (ii) their highly anisotropic textures with weak gradients along the material directions $\mathbf{e}_I, \mathbf{e}_{II}$ but also (iii) the highly heterogeneous deformation field together with (iv) the large geometrical transformations induced by the bias-extension loading mode. To address the resulting issues, we developed a dedicated two-step DVC procedure which is detailed hereafter and illustrated schematically in Fig. 4.

3.2.1. Step 1 – Initial guess

As a first step, an initial first order guess of the displacement field between two configurations was estimated based on the procedure proposed in [44]. A set of "guiding points" was selected in the reference image, which exhibits numerous zones with large grey level gradients (see Fig. 4a). This selection was based on a 3D Harris corner detection algorithm [45] while a minimum distance between the selected points was also imposed. The higher the Harris' corner value (*i.e.*, absolute value of the smallest eigenvalue of the auto-correlation matrix), the higher the quality of the imaged pattern for the correlation purpose.

The displacements of the guiding points were then measured from the reference to the deformed configuration based on a coarse nearest-pixel cross-correlation computation. For this, a local sub-volume (*i.e.*, correlation window) was extracted around each guiding point in the reference image (see square in Fig. 4a). The displacement of each guiding point was then determined by finding the best mapping of the extracted sub-volume in the deformed image, searching over a restricted "search window". This mapping corresponds to the highest normalized cross correlation coefficient corrected by the average intensity of each image [46]. The choice of the correlation window size was based on the structure of the material, while the size of the search window was based on the estimated expected deformation. Note that even though an heterogeneous deformation field was expected, the search window was kept constant for all guiding points.

The feature, however, which was unique for each guiding point was the "guessed" position around which it is sought in the deformed configuration, which is actually the key component of this procedure. More specifically, the key of this initial step lies in the fact that the tracking of the guiding points was *progressively* done inside the sample by propagating the motion of neighboring points. For this, guiding points were sorted in a queue based on their distance to any point of the queue (*i.e.*, the point closest to any point of the queue was the next one to be en-queued). Each point was then sought around a "guessed position" in the deformed configuration, which was defined based on the tracked position of previously successfully correlated neighboring guiding points. It is important to note that for the first point no initial estimation was given (*i.e.*, the "guessed position" was equal to its position in the reference configuration) and its correlation coefficient was directly calculated. Consequently, the selection of the first guiding point (*i.e.*, top of the queue) is crucial for the success of this procedure and should be based on some *a priori* estimation of the displacement of certain parts of the specimen. Here, a point that lies in the region close to the top clamp (and thus with a very small expected displacement) was chosen, which is not necessarily the one with the highest Harris' corner value.

For each of the remaining sorted points, a "guessed position" in the deformed image was estimated by a Gaussian distance-based weighted interpolation of the measured displacements of neighboring guiding points. Neighbors only within a given distance of the currently processed point were considered, for which the previously calculated correlation coefficient was higher than a threshold (herein set to 0.98, *i.e.*, a correlation coefficient of 1.0 implies that the sub-volumes are completely related). After processing the entire queue, the guiding points displacements were available (see Fig. 4c), with the quality of the measurement assessed by their corresponding correlation coefficients.

3.2.2. Step 2 – Regular DVC

Step 1 provided a rough estimate of the (guess point) displacement field with a 1-pixel sensitivity. This field was then interpolated to a set of points laid in a structured grid (see Fig. 4e), providing a good displacement guess for a local DVC computation, as implemented in the open source software spam [47]. For this, a regular grid of points was used by subdividing the reference image into a set of independent sub-volumes, *i.e.*, correlation windows, which were sought in the deformed image (see Fig. 4d). At the center of each correlation window a linear and homogeneous transformation function $\boldsymbol{\Phi}$ was estimated such that the material point in the position $\mathbf{x}$ in the reference sub-volume corresponded to the same material point in the position
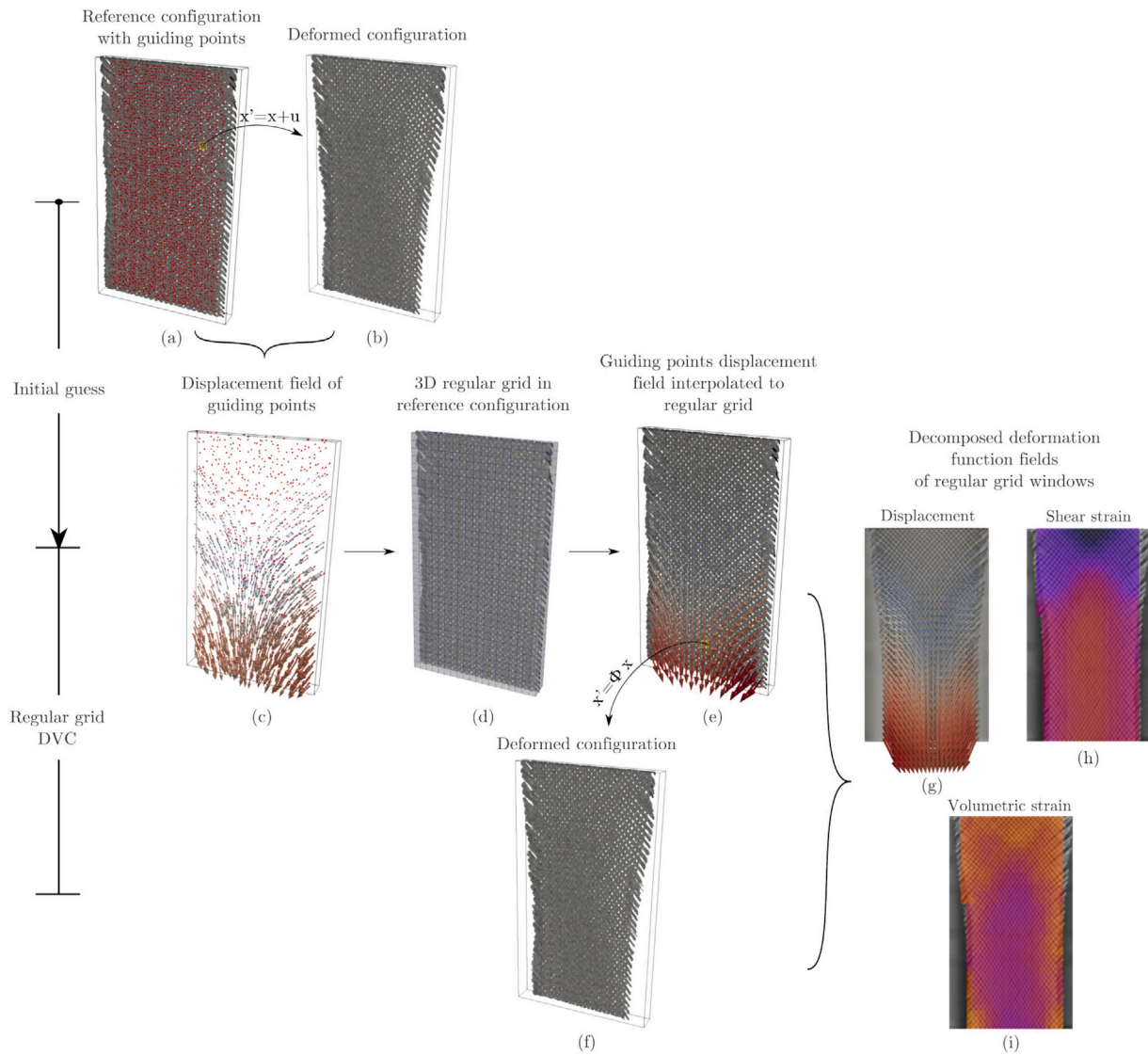
Fig. 4. Flowchart of the developed two-step DVC procedure.

$\mathbf{x}' = \boldsymbol{\Phi} \cdot \mathbf{x}$ in the deformed sub-volume (see Fig. 4e–f). Note that the transformation function $\boldsymbol{\Phi}$ in spam is represented by a 4×4 matrix that accounts for affine transformations: displacement, rotation, normal and shear deformation. The first three rows of the fourth column of $\boldsymbol{\Phi}$ describe rigid-body displacements, while the top corner 3×3 sub-matrix corresponds to the familiar, from continuum mechanics, deformation gradient tensor, $\mathbf{F}$. This means that unlike typical local DVC approaches, *non-rigid* correlation windows were used here directly measuring local rotations and strains.

The formulation of the correlation procedure in spam is based on a *gradient-based* iterative algorithm using a first-order Taylor expansion that minimizes the Sum of Square Differences (SSD) between the reference and the deformed sub-volume, the latter being corrected by a trial deformation function [48–50]. The convergence criterion is based on the norm of the deformation function increment between two successive iteration steps, while a maximum number of iterations is also set as a limit to stop the iterative procedure in the case that the convergence criterion is not satisfied.

Note that for large deformations, which happens to be the studied case, the convergence of the iterative algorithm might be difficult, since the applicability of the first-order Taylor expansion is questionable. This means that a direct implementation of the above "local" DVC procedure would be rather ill-fated, since the gradient-based algorithm

would fail to converge, unless the initialization of the transformation function $\boldsymbol{\Phi}$ for each local sub-volume computation would be close to the right solution. This is exactly why the "guiding points" displacement field was used. As it was interpolated to the points of the structured grid (see Fig. 4e), it provided a good displacement guess for the local computations, thus driving the gradient-based local algorithm to a good solution.

3.2.3. DVC parameters and procedure

For the initial guess of Step 1, the size of both the correlation and search windows were selected as anisotropic (smaller value in the thickness direction), reflecting the texture anisotropy and the geometry of the basalt textile and the larger in-plane deformation, respectively. More precisely, a $31 \times 31 \times 21$ voxels correlation window and a $15 \times 15 \times 7$ voxels search window were used. For the iterative algorithm of Step 2, the norm of the transformation function increment was set as $\|\Delta\boldsymbol{\Phi}\| < 10^{-4}$, while a maximum number of 200 iterations was chosen. In addition, due to the slenderness of the woven sample, only one grid point was used along the thickness direction. Regarding the in-plane grid, contiguous (point spacing equal to window size) square correlation windows were used, ensuring a statistical independence of the corresponding error [51]. The size of the in-plane squares was set
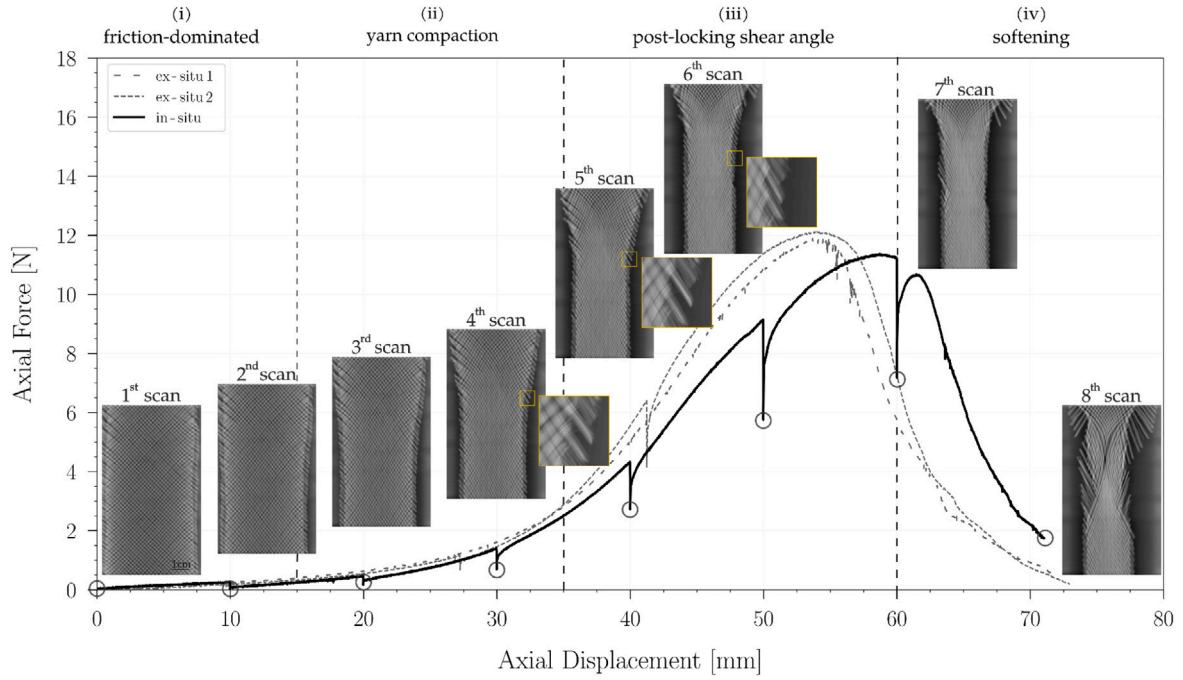
Fig. 5. Macroscopic force–displacement curve of the bias-extension test performed *in situ* in the X-ray tomograph, along with the enhanced radiographs (*i.e.*, reconstructed projections averaged in the thickness direction) of each scan. The zoomed images show that slipping bundles can be identified from the 6th step and inwards.

to 91^2 pixels (*i.e.*, 2.73×2.73 mm^2) based on a DVC measurement uncertainty analysis with a "zoomed out" scan, as detailed in Appendix B. Note that all DVC measurements presented in the following are accompanied by a relative error, calculated through the aforementioned uncertainty analysis.

It is important to stress here that the positions of the guiding points of Step 1 were defined at the reference scan and were incrementally tracked between two successive scans. Similarly, an incremental analysis was performed for the DVC calculations of Step 2: a new grid of points was defined for each pair of images to be correlated and the displacements of the incrementally tracked guiding points were interpolated to the grid positions. The application of the iterative procedure described above was used to compute the 3D incremental deformation gradient $\delta\mathbf{F}_{t_i - t_{i+1}}$ for each correlation window and thus a 3D map of the incremental deformation gradients for the whole image. A multiplicative composition of the incremental deformation gradients produced the total deformation gradients $\mathbf{F}_{t_0 - t_i}$ (further noted $\mathbf{F}$) that mapped the grid points of the reference scan into each of the subsequent scans captured throughout the experiment. To ensure the applicability of the incremental multiplicative composition, we checked that the deformation field coming from the correlation of the reference with the third scan corresponded to the deformation field coming from a multiplicative composition between the reference and the second scans, followed by the second and the third scans.

3.2.4. Fiber orientation, shear angle and natural strain invariants
We used the above two-step DVC procedure to estimate:

- The local orientation of the weft ($i = I$) and the warp ($i = II$): $\mathbf{e}_i = \mathbf{F} \cdot \mathbf{e}_i^0 / \|\mathbf{F} \cdot \mathbf{e}_i^0\|$, where the $\mathbf{e}_i^0$ were estimated with OrientationJ in the reference configuration.
- The local shear angle $\gamma = \pi/2 - \arccos(\mathbf{e}_I \cdot \mathbf{e}_{II})$.

We also computed 3D maps of the 3D natural (or the Hencky) strain tensor $\boldsymbol{\varepsilon} = \ln(\mathbf{F} \cdot \mathbf{F}^t)/2$ and its in-plane projection $\tilde{\boldsymbol{\varepsilon}} = \boldsymbol{\varepsilon} \cdot (\boldsymbol{\delta} - (\boldsymbol{\pi} + \boldsymbol{\pi}^t)/2)$, where $\boldsymbol{\delta}$ is the identity tensor, $\boldsymbol{\pi} = (\mathbf{e}_\alpha + \mathbf{e}_\beta + \mathbf{e}_{III}) \otimes \mathbf{e}_{III}$ and where $\mathbf{e}_\alpha$ and $\mathbf{e}_\beta$ are two unit vectors perpendicular to the out-of-plane unit vector $\mathbf{e}_{III}$. Therewith, some physically relevant natural strain invariants were estimated, accounting for (i) the evolving twill anisotropy

characterized by the material directions $\mathbf{e}_I$, $\mathbf{e}_{II}$, $\mathbf{e}_{III}$, as well as (ii) the main deformation mechanisms observed during the bias-extension test:

- The volumetric strain $\varepsilon_v = \boldsymbol{\varepsilon} : \boldsymbol{\delta}$, where $\boldsymbol{\delta}$ is the identity tensor,
- The elongation strains $\varepsilon_i = \mathbf{e}_i \cdot \boldsymbol{\varepsilon} \cdot \mathbf{e}_i$ along the weft ($i = I$), the warp ($i = II$) and the twill thickness ($i = III$) directions,
- The equivalent in-plane shear (or deviatoric) strain $\tilde{\varepsilon}_{eq} = \sqrt{\frac{2}{3}(\tilde{\boldsymbol{\varepsilon}} : \tilde{\boldsymbol{\varepsilon}} - \varepsilon_s^2)}$, where $\varepsilon_s = \varepsilon_v - \varepsilon_{III}$ is the in-plane surface strain.

As an example, the decomposed total displacement field, along with the volumetric strain ε_v and the equivalent in-plane shear strain $\tilde{\varepsilon}_{eq}$ have been reported in Fig. 4g–i.

4. Results and discussion

4.1. Force–displacement curve and shear angle

The force–displacement curve measured during the *in situ* test is shown in Fig. 5. The loading steps after which the scans were carried out are indicated in the figure, along with the enhanced radiographs of each scan (*i.e.*, reconstructed projections averaged in the thickness direction). Note that a significant deformation of the woven fabric sample can be seen in these images, the quantification of which will be discussed in the following paragraphs and subsections. The figure also brings up the following remarks:

- A typical pronounced force relaxation is observed each time the loading is interrupted for the X-ray acquisition ($\approx$20–30% of the maximum force reached before the interruption). This phenomenon is commonly observed with fibrous materials [52] and may be ascribed to small rearrangements at the fiber–fiber contact scale. However, it is worth noting that the test interruption and the related sample relaxations do not affect the global mechanical behavior of the sample. Indeed, reloading the sample after relaxation allows the force–displacement curve to return back onto its initial loading path, which is very similar to those obtained from the samples loaded without interruption (see the dashed lines in the same figure).

- The recorded force–displacement curves are in-line with the literature data and can be divided into four distinct regions [2,22,53]: (i) the friction-dominated region at low displacement (scans 1–2); (ii) the yarn deformation region, where the slope increases with the displacement (scans 3–4); (iii) the post-locking shear angle region with a sharp increase in load until the peak (scans 5–6); and finally (iv) a softening region until breakage (scans 7–8).
- As shown in the zoomed images, it is important to stress that no yarn slippage is visible during the first five steps, while this phenomenon can be detected in the enhanced radiograph of the 6th step. This observation signifies that the condition of the material continuity assumed in the DVC measurements (and most of the continuum modeling approaches of the literature) is not strictly satisfied from the sixth step and onwards. There, the warp and the weft yarns should then be considered as distinct and interacting continuous media [54]. Unfortunately, the warp and weft separation (*e.g.*, thresholded based on their different orientation) was not possible with our 3D images due to the scanning spatial resolution and the high shear the fabric was subjected to: as stated in [10,55], we assumed that the yarn slippage above the 5th step was limited, so that a one-phase continuous approach could still be used.
- The comparison of the evolution of the theoretical (*cf.* Eq. (1)) and the measured shear angles (using either OrientationJ or DVC, see Section 2) inside the central region D is reported in Fig. 6. As expected for the reference scan (*i.e.*, at zero axial displacement), the mean orientation angles of the warp and weft are 45° and −45°, respectively, resulting to an initial mean shear angle equal to zero. As the axial load increases, the shear angle γ increases. It is interesting to notice that the values measured through the orientation tensor are in a good agreement with the ones assessed through DVC (these values were also manually recovered by directly measuring by hand the angles between the warp and the weft on the central region of the enhanced radiographs). The maximal measured shear angle is 65°, a value which indicates that the sample was subjected to large shear deformation. Furthermore, the theoretical angle prediction is in good accordance with the experimental data up to a "locking" value of $\approx 30°$, which is in-line with the results reported in the literature for glass plain woven textiles, carbon fabrics and unbalanced twill weave fabrics [2,3,7,56]. Above the locking angle, the simplifying assumptions stated in Eq. (1) are not valid, in particular due to the compaction and the twist of the cross sections of the fiber yarns induced both by steric hindrance and their high transverse deformability [8,9], their possible (un)folding and in-plane bending upon loading and, after the 5th step, yarn-yarn slippage. Apart from the yarn-yarn slippage, these effects will be discussed in the next subsection.

4.2. Kinematic fields

4.2.1. General trends

Fig. 7 gathers a number of colormaps showing the time-evolution of the displacement field, together with three key strain invariant fields: the equivalent in-plane shear strain $\tilde{\varepsilon}_{eq}$, the volumetric strain ε_v and the out-of-plane strain ε_{III}. This figure brings up the following comments:

- During the first loading step, a smooth distribution is observed in all the reported kinematic fields. Note that the displacement vectors point downwards, thus indicating the direction of the applied tensile load (see Fig. 3). As the global displacement d increases (and thus the shear angle γ), the magnitudes of the local displacements vectors are progressively increasing from the top (almost zero displacement) to the bottom of the imaged zones (which is the middle part of the scanned sample). Furthermore, the displacement field is becoming more irregular as the test is pursued, suggesting the existence of different deformation zones, which are characteristic of the bias-extension test.
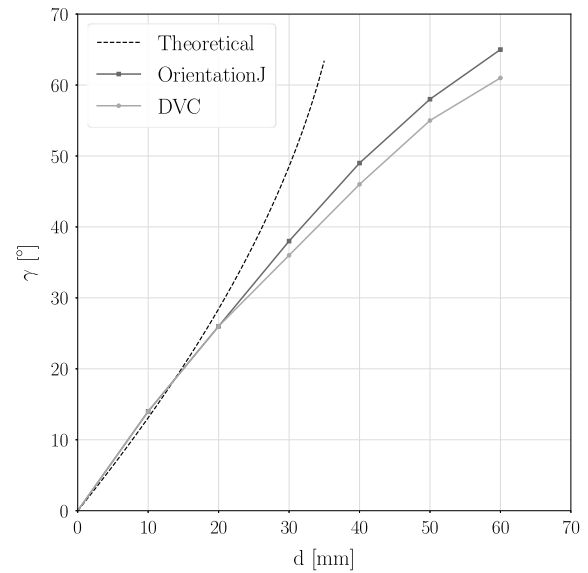

Fig. 6. Evolution of theoretical and measured shear angles γ in the central region D of the sample as a function of the displacement d.

- The deformation zones A, B, C and D defined in Fig. 1 can be clearly identified in the in-plane shear strain field maps (see Fig. 7(b)) with shear strain values $\tilde{\varepsilon}_{eq}$ inside each zone remaining more or less constant, *i.e.*, more or less in accordance with the theoretical geometrical assumptions used to establish Eq. (1). Zone A, at the top of the sample, exhibits very small strains compared to the other zones. This is attributed to the fact that both warp and weft yarns are fixed at the upper rigid clamp. It is worth noting that the strains inside this region are not strictly zero-valued as suggested by the theoretical geometrical approach. This is partly due to the fact that the reconstructed volume is cropped slightly away from the top border of the sample, but also to internal length effects which will be discussed later. The central zone D exhibits the largest shear strain with practically homogeneous strain field except free edge effects. Two relatively symmetric intermediate zones B and C can also be identified, between those measured for zones A and D, where the shear strain is practically equal. It is important to mention that all the transitions between these zones do exhibit finite lengths, which is in-line with the experimental literature data and far from the theoretical geometrical approach.
- The values reported for the in-plane equivalent shear strain $\tilde{\varepsilon}_{eq}$ are higher than those recorded for the other strain invariants. This indicates once again that the sample is mainly subjected to large shear deformation. In addition, close to the force peak (see steps 6 and 7), one can notice that high shear strains are concentrated in a relative narrow band between the intermediate zones (B,C) and zone (D). This region of sudden localized deformation coincides well with the location where the material finally tears apart, as shown with the enhanced radiograph of the post-peak scan (see scan 8 of Fig. 5).
- The in-plane shear strain field discussed above is a field quantity broadly studied for the analysis of the in-plane shear properties of woven textiles, in particular during bias-extension. Likewise, the shear angle, and in a less extent the lateral in-plane strains are also widely studied, especially when optical measurements of the sample's surface are available. Beyond these in-plane measurements, the *in situ* test presented herein coupled with the proposed DVC methodology give access to the measurement of 3D strain fields, such as those reported in Fig. 7(c–d), *i.e.*, quantities which (i) have never been quantified up to date and (ii) are
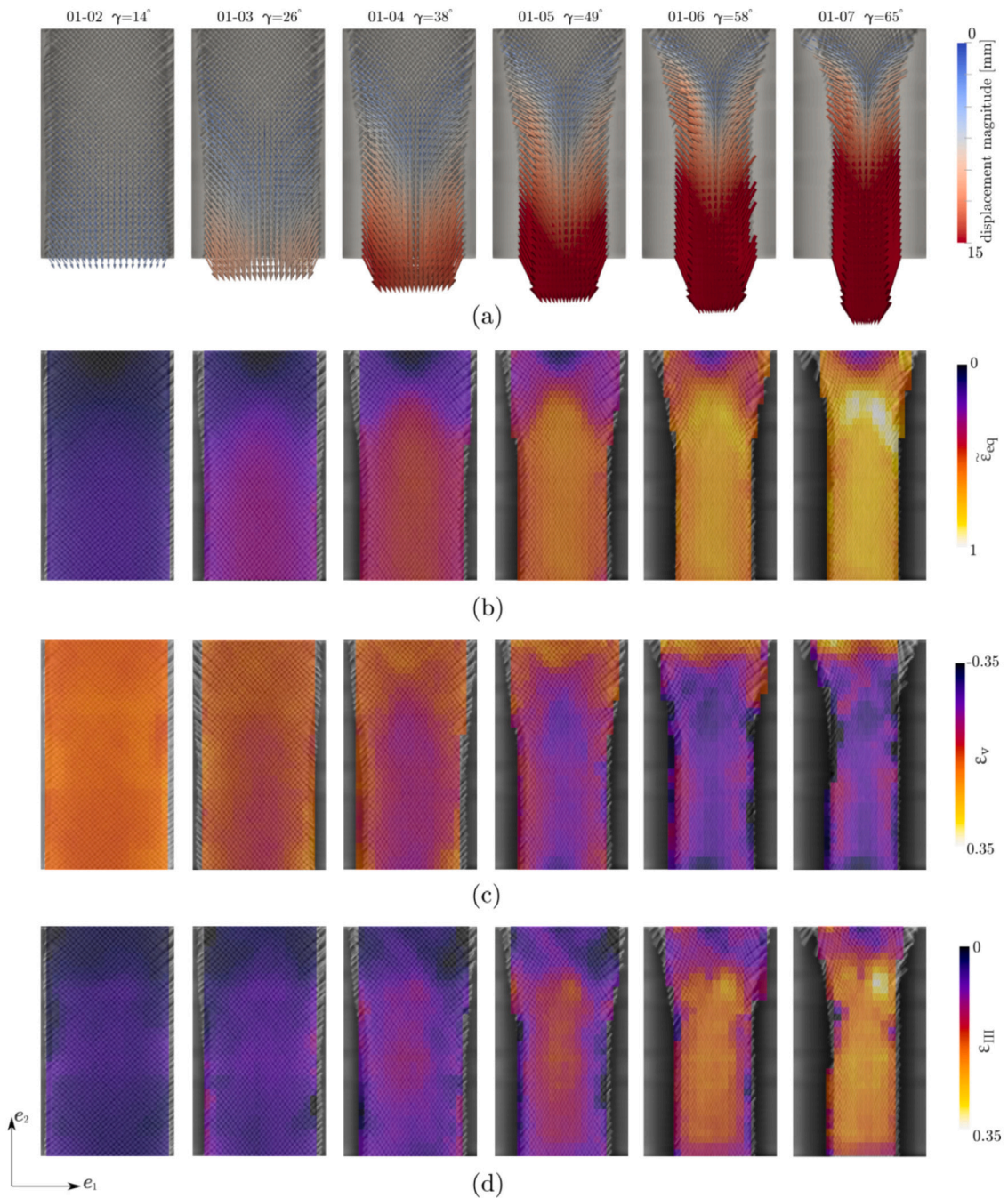
Fig. 7. Half-sample upper views (parallel to $\mathbf{e}_{III}^0$) and related colormaps showing the time evolution of 3D displacement field (a), the in-plane equivalent shear strain $\tilde{\varepsilon}_{eq}$ (b), the volumetric strain ε_v (c), and the out-of-plane strain ε_{III} (d) during the *in situ* test.

rarely taken into account in existing constitutive schemes. For example, the colormaps in Fig. 7(c) show that the volumetric strain ε_v is significant and mostly negative, reaching low negative values of $\approx -25\%$, thus proving that the tested woven fabric is also subjected to a pronounced compaction, which is in turn expected to induce a severe increase of the fiber content ϕ in the sample of $\approx 28\%$ (since $\phi/\phi^0 = \mathrm{e}^{-\varepsilon_v}$). Astonishingly, Fig. 7(d) proves that meanwhile, a considerable dilation, *i.e.*, a marked auxetic effect reaching $\approx 25\%$ is measured for the out-of-plane strain field ε_{III} (note that such a directional dilatant behavior is also confirmed by the evolution of the local thickness map, see Appendix B). Consequently, these two remarks highlight the high anisotropic compaction of the sheared twill during bias-extension, *i.e.*, with noticeable out-of-plane auxetic effects that are largely

compensated by pronounced in-plane compaction surface strain $\varepsilon_s = \varepsilon_v - \varepsilon_{III} \approx -50\%$. In addition, these results also question the relevance of the expression "pure shear" deformation which is often associated with the bias-extension test, *i.e.*, a deformation mode involving the distortion of the material reference frame $(\mathbf{e}_I^0, \mathbf{e}_{II}^0, \mathbf{e}_{III}^0)$ only. Fig. 7 proves that other deformation mechanisms are involved, including at least (see next subsection) volumetric and out-of-plane strains. This point is valid even before the locking angle: within this shear angle range, not only an in-plane shear is observed, but also a non negligible out-of-plane strain (see the two first colormaps of Fig. 7(b) and (d), respectively). Lastly, these data provide novel valuable insights into the actual 3D mechanics of the material, which are particularly useful for theoretical and numerical models of woven fabrics.

4.2.2. Strain paths in "homogeneous zones"

To further investigate strain fields and their complex coupling, we have reported in Fig. 8 the evolution of the mean values of the in-plane shear strain $\tilde{\varepsilon}_{eq}$, the volumetric strain ε_v, the out-of-plane strain ε_{III} and the elongation strains along the weft ε_I and the warp ε_{II} directions, as functions of the shear angle γ and for the four characteristic zones A, B, C, D (see Fig. 1). This figure conjures up the following comments:

- Independently of the considered strain invariant, these results prove again that region D exhibits the highest strain values, with regions B and C exhibiting intermediate values, while region A the lowest. One can notice that the shear strains $\tilde{\varepsilon}_{eq}$ in zones B and C are not exactly twice as low as the values reported in zone D. As it will be seen in the next subsection, this may be due to the fact that the small areas used here to average strain fields in zones B and C (see Fig. 1) are not small enough not to account for strain gradients between them and zone A.

- For each strain invariant, the values reported in zone B are close to those reported in zone C. We also noticed previously that the mean orientation angles of the warp and weft were initially 45° and −45°, *i.e.*, symmetrically, with respect to the loading axis. These two remarks show that upon loading, the weft and warp orientation and their related deformation should still remain symmetric, as expected for such an initial balanced configuration.

- Fig. 8(b) highlights the marked compaction the fabric is subjected to in zone D. For the deformation region (i), *i.e.*, when $0° \leq \gamma \leq 20°$ (see Fig. 5), this compaction is limited (the volumetric strain ε_v is close to 0) so that any variation of the fiber content should not occur at the macroscale. Above, the decrease of ε_v is marked ($\approx -\tilde{\varepsilon}_{eq}/4$) and thus the increase of the fiber content ϕ. The volumetric strain ε_v evolves practically linearly up to the end of region (iii). This compaction and its impact on the fiber content cannot be neglected. Its origins are multiple, multiscale, intricate, with sometimes opposite effects. One of the major compaction mechanisms is the increase of the shear angle γ which yields to a decrease of the in-plane surface strain ε_s, and thus of the volumetric strain ε_v. At the microscale, the reorganization of the filaments inside the yarns should also yield to the compaction of the yarn cross sections [8,9], and thus to the observed macroscopic compaction. Two other origins are described and discussed in the two following points.

- As depicted in Fig. 8(d,e), we measured rather small ($\approx \tilde{\varepsilon}_{eq}/10$) but non-negligible macroscopic positive tensile strains along the weft and the warp directions, both reaching $\approx 8\%$ at the end of the test in zone D (note that a segmentation by hand of a set of fiber bundles confirmed this extension, even though the error of this hand-based operation can be relatively high). This macroscopic tension mode is probably induced by the yarn longitudinal unfolding at the mesoscale. In contrast with the effect induced by the shear angle, the recorded tensile strains should induce an increase of the in-plane surface strain ε_s and thus of the volumetric strain ε_v.

- A noticeable out-of-plane auxetic effect is observed during the test and more precisely in zone D, where the out-of-plane strain ε_{III} increases practically linearly with significant values ($\approx \tilde{\varepsilon}_{eq}/4$) up to $\approx 22\%$ (Fig. 8(c)). This effect has already been observed in other fibrous materials such as textiles, papers, self-entangled filaments [57–59]: yarn-yarn steric hindrance, yarn curvature and transverse twisting are possible mesoscale mechanisms that could explain the auxetic behavior observed at the macroscale [8,58]. As for the previous deformation mode, the contribution of the auxetic effect on the volumetric strain ε_v restrains the fabric compaction. Thus, during the deformation stage (i), *i.e.*, when $0° \leq \gamma \leq 20°$, the volumetric strain ε_v is practically zero-valued (Fig. 8(b)): the positive in-plane tensile strains ε_I and ε_{II} together with the positive out-of-plane strain ε_{III} completely anneal the compaction

induced both by the shear angle increase and the microscale filament reorganization. Such an effect vanishes for the remaining deformations stages, with the two previous mechanisms being much more pronounced.

- We have reported in the 3D graph of Fig. 8(f) the strain paths $(\tilde{\varepsilon}_{eq}, \varepsilon_v, \varepsilon_{III})$ recorded in zones A, B, C, D. Firstly, by assuming that the weft and warp strains can be neglected as a first rough approximation (due to their much lower values), this graph shows that very similar strain paths are followed independently of the considered zone. Secondly, the graph highlights the strong coupling of the strain deformation modes. On the one hand, such a complex coupling must be taken into account for modeling approaches: to the best of our knowledge, this is not the case at the moment. On the other hand, this coupling should presumably be altered by (even slight) modifications of the boundary conditions of the test, *e.g.*, closer to those encountered during fabric forming processes (stamping, compression...): in-plane constraints such as tension on yarns [60], out-of-plane compression and shear. This open hypothesis requires additional experiments to be carried out.

4.2.3. Strain and strain gradient profiles along transition zones

The 2D experimental observations of the literature proved that transition zones between the sheared zones A, B, C, D are not abrupt but exhibit bands of finite widths [2,4,7]. These macroscopic bands are correlated both to the poor scale separation between the macroscopic (sample) and the mesoscopic (yarn) scales and to the non-zero bending stiffnesses of the yarns that induces smooth transitions of the macroscopic fields. To complement and enhance quantitatively these results, we have reported in Fig. 9 the profiles at various shear angles γ of the key strain invariants $\tilde{\varepsilon}_{eq}$, ε_v and ε_{III} along lines initially perpendicular to the transition zones B–D, as sketched in Fig. 1. A similar figure is proposed along the line perpendicular to the transition zones A–B in Appendix C (see Fig. C.13). The strain profiles have been plotted as functions of the dimensionless variable $s^* = s/\lambda$, s is the curvilinear abscissa of the line and λ the in-plane length of the periodic Representative Elementary Volume (REV) of the fabric (see Fig. 2). From this figure (and Fig. C.13), it is clear that along the plotted profiles there is a gradual transition which increases as the test evolves, independently of the considered profile line and strain invariant. The width of the transitions zones is well-identified: it does not depend on the strain invariant nor on the profile line, being about 2 to 3 times the length λ of the fabric REV, thus emphasizing the influence of the mesostructure on the fabric macroscopic 3D strain fields. Note that similar internal length effects have been found in other discrete systems, *e.g.*, during the compression of granular geomaterials with the occurrence of well-known shear bands the width of which extends in the order of a few grains [61].

It is also worth mentioning that the observed internal length effects are not taken into account in the standard geometrical framework used to analyze the bias-extension test [5]. In addition, these effects cannot be captured when using the set of macroscopic mechanical models of the literature which are based on a standard Cauchy continuum assumption. Novel strategies based on generalized continuum approaches such as second gradient models have been developed purposely, but still lack quantitative experimental data to be properly built and calibrated [11,12,62,63]. For example, the second gradient hyperelastic model reported in [63] suggests that the strain energy can be a function of the gradient of the shear strain, accounting for the local in-plane curvature of the continuum (and thus the yarn bending). Following this approach, we computed the gradient of the in-plane deviatoric shear strain along the transition zones, $\nabla_s \tilde{\varepsilon}_{eq} = \partial \tilde{\varepsilon}_{eq}/\partial s$, and plotted its evolution in Fig. 9 for line B–D (and for line A–B in Appendix C). Thanks to the 3D images and the DVC measurements, we also computed the gradients of other strain invariants such as $\nabla_s \varepsilon_v$ and $\nabla_s \varepsilon_{III}$ (see the same figures): as the observed auxetic and compaction effects should
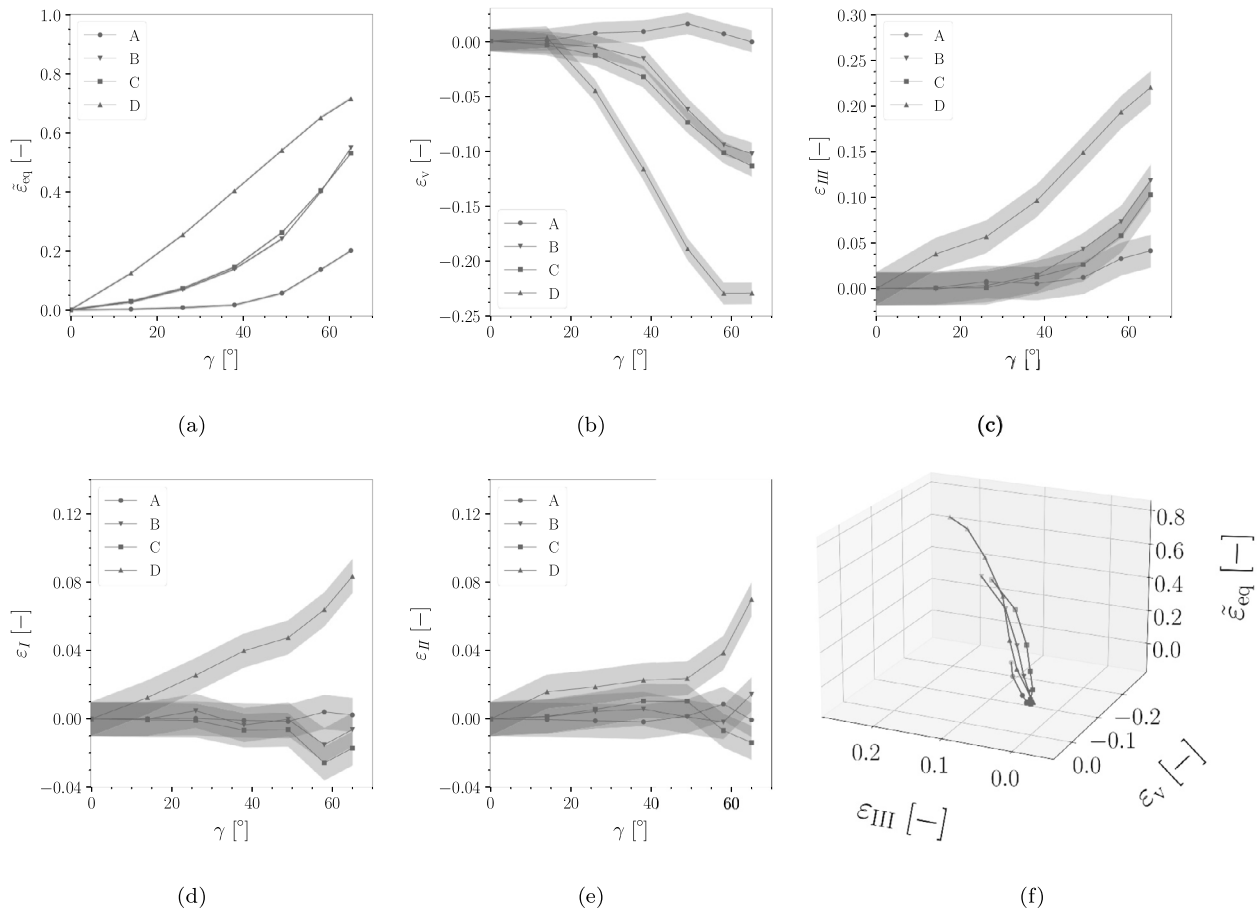
Fig. 8. Evolution of the mean values of the in-plane equivalent shear strain $\tilde{\varepsilon}_{eq}$ (a), the volumetric strain ε_v (b), the out-of-plane strain ε_{III} (c) and the elongation strains along the weft ε_I (d) and the warp ε_{II} (e) directions, as functions of the shear angle γ and for the four characteristic zones A, B, C, D, (*i.e.*, the characteristic regions that are sketched in Fig. 1). Note that shaded areas around the solid lines correspond to the DVC measurement errors calculated through the uncertainty analysis detailed in Appendix B. Graph (f) gives the same strain paths in the ($\tilde{\varepsilon}_{eq}$, ε_v, ε_{III}) space.

partly be induced by the twisting and the out-of-plane bending of yarns, these gradients may also be relevant quantities for the formulation of second gradient models. Within a bandwidth similar to that observed for the respective strain invariants, Fig. 9 highlights the sharp evolution of the second gradient of the reported strains. In particular, it is interesting to note that the evolution recorded for $\nabla_s \tilde{\varepsilon}_{eq}$ is very similar to that exhibited by the in-plane yarn curvatures, which were assessed by tracking manually the yarn centerlines along the transition zones in the enhanced radiographs (see Fig. C.14 in Appendix C).

5. Conclusion

In this study, we presented novel experimental data that were acquired during the *in situ* X-ray bias-extension of a thin balanced twill fabric. A experimental set-up compatible with a laboratory X-ray microtomograph was developed purposely. Beyond the standard in-plane analysis of a bias-extension test, the main goal of this work was the quantification of the full 3D strain field of the deformed textile thanks to a DVC analysis of the 3D images acquired during the *in situ* test. The measurement of the 3D kinematic fields was an intrinsically a challenging task, due to the quasi-periodic architecture of the textile, its highly anisotropic texture, but also the complex large deformations with strain localization the textile was subjected to. To overcome these bottlenecks, a dedicated DVC procedure was proposed, the key feature of which was the gradual propagation throughout the specimen of selected guiding points that were used as a proper initial displacement

guess to a regularly-spaced "local" DVC computation. This method delivered interesting experimental results that are summarized in the following points:

- The macroscopic response exhibited a typical J-shaped force–displacement curve. Yarn slippage was observed only at the end of the test, implying that the material continuity condition assumed in the DVC measurements was satisfied for all of the previous loading steps.
- The measurement of the shear angle (that reached 65° at the end of the test) through the acquired images was necessary, since, as expected, the geometrical prediction overestimated the actual measurement above the locking angle of $\approx$30°. This measurement can be fairly well estimated from the knowledge of the initial orientation vector of the weft and the warp and by simply convecting these vectors with the gradient of the transformation deduced from DVC measurements.
- In accordance with the standard geometrical assumptions, the bias-extension generated large shear strains of the fabric with three distinct deformation regions exhibiting roughly constant strain values. The 3D images coupled with DVC proved that the bias-extension is not restricted to pure shear deformation, even before the locking angle: other important deformation modes occurred, such as the fabric compaction, out-of-plane auxetic effects, and in-plane yarn expansion. Similarly with the shear strain, these deformation modes were rather constant inside the characteristic zones.
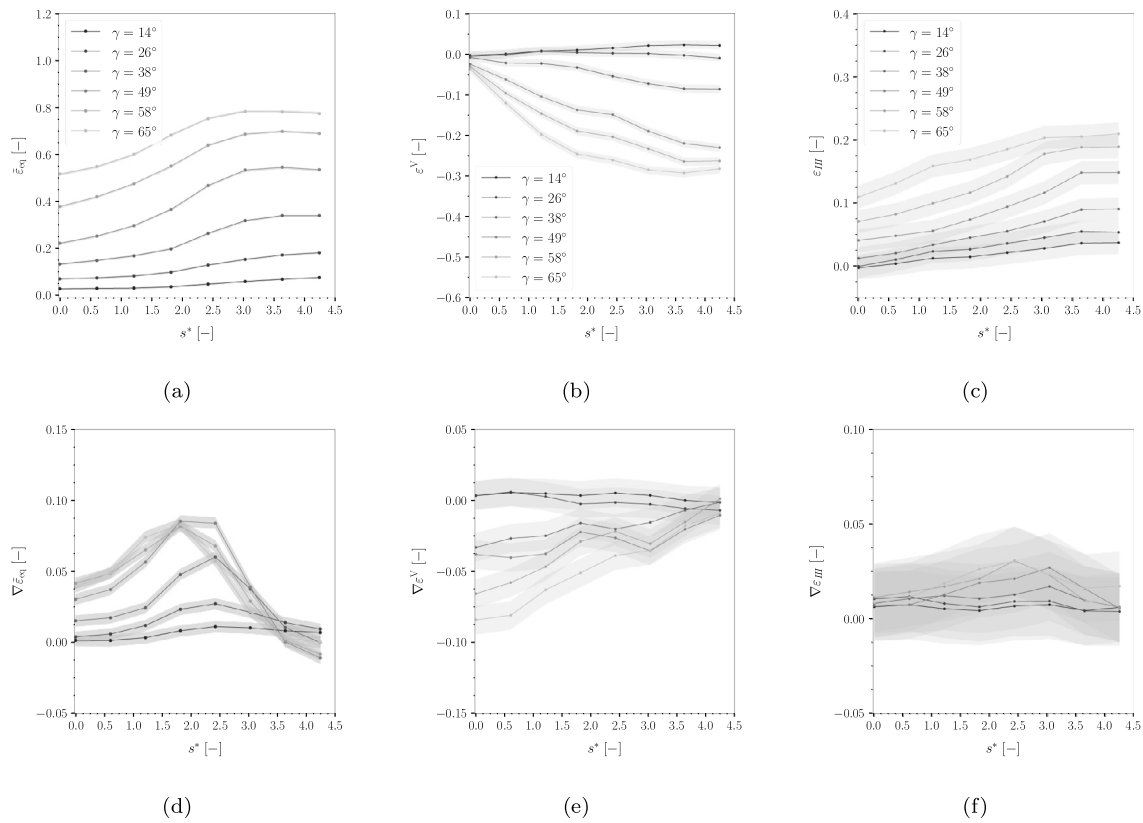
Fig. 9. Evolution of in-plane equivalent shear strain $\tilde{\varepsilon}_{eq}$ (a), the volumetric strain ε_v (b) and the out-of-plane strain ε_{III} (c) along the adjacent region B–D (the path is sketched in Fig. 1), together with their respective gradients $\nabla_s \tilde{\varepsilon}_{eq}$ (d), $\nabla_s \varepsilon_v$ (e) and $\nabla_s \varepsilon_{III}$ as functions of the dimensionless curvilinear abscissa s^*. Note that $s^* = 0$ is at region B.

- Albeit rarely characterized, discussed and taken into account in existing constitutive schemes, the volumetric strain field indicated an important compaction of the fabric upon loading (reaching 30%). This compaction induced a severe increase of the fiber content in the fabric. It is, in fact, a complex combination of antagonistic deformation mechanisms induced by the multiscale and highly anisotropic architecture of the fabric: (i) compaction enhanced by the increase of the shear angle and thus a pronounced decrease of the in-plane surface strain together with yarn compaction (especially above the locking angle), (ii) dilation induced by a marked out-of-plane auxetic expansion and a limited in-plane yarn unfolding. In order to better understand these deformation mechanisms, a multiscale study is required. Combined with the textile scale analysis presented herein, additional and simultaneous analyses at the yarn and the filament scales will allow to unravel quantitatively the coupled effects related to the textile elongation/compaction/shear to those related to the yarn compaction/torsion/tension/bending [8] to those related to the filament rearrangement and bending [9].

- In contrast with the standard geometrical assumptions, but in accordance with previous experimental evidences, we showed that the transition between the characteristic zones was smooth. This transition occurred in a region with a band-width close to 2–3 REV size, regardless of the considered strain invariant. The results gathered in this study thus reinforce and complete experimental observations already reported in the literature. They highlight internal length effects which are (i) observable due to a poor scale separation between the macro and the mesoscale and (ii) due to the finite bending and twisting stiffnesses of fiber yarns. They question the relevance of standard Cauchy continuum-based models which cannot reproduce them. On the

contrary, these results encourage the development of models in the framework of generalized continuum mechanics, such as the second gradient models recently proposed in the literature. In this context, by extracting some interesting gradients of the strain invariants from the 3D strain fields, this study also demonstrated that the combination of X-ray tomography and DVC could be an interesting experimental investigation method to build and validate macroscopic models with enriched kinematic fields.

- A number of important in-plane observations can be measured during a standard bias-extension test. Other relevant information can also be obtained from this test using 3D imaging (X-ray tomography) or 2.5D imaging (stereo digital image correlation). However, one should be aware of the (i) out-of-plane kinematical constraints (mould contact/closure) but also the (ii) in-plane mechanical/kinematical constraints (such as those investigated in [60]) a textile is subjected to during its forming. Both are not active during the bias-extension and should require further investigations.

CRediT authorship contribution statement

O. Stamati: Conceptualization, Methodology, Software, Investigation, Writing – original draft. **L. Orgéas:** Conceptualization, Methodology, Writing – review & editing, Supervision, Funding acquisition. **S. Rolland du Roscoat:** Conceptualization, Writing – review & editing. **P. Lhuissier:** Methodology, Software, Writing – review & editing. **P.J.J. Dumont:** Conceptualization, Methodology, Writing – review & editing. **F. Martoïa:** Conceptualization, Methodology, Writing – review & editing.
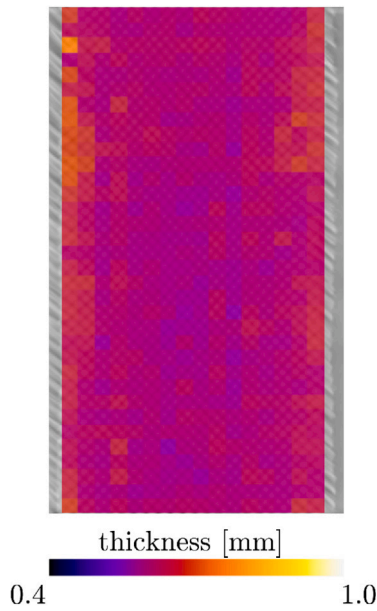
Fig. A.10. Thickness map of the studied textile in the reference configuration, estimated with the method reported in Section 3.1.

Declaration of competing interest

The authors declare the following financial interests/personal relationships which may be considered as potential competing interests: Orgeas reports financial support was provided by French National Research Agency.

Data availability

Data will be made available on request.

Acknowledgments

Appendix A. Thickness of the textile

See Fig. A.10.

Appendix B. DVC measurements uncertainties

To quantify the measurements uncertainties of the applied DVC procedure, a "zoomed out" scan was performed before starting the *in situ* test. This scan was acquired after a 6.3% demagnification obtained by translating the sample closer to the detector, decreasing the voxel size from 30 (during the *in situ* test) to 32 μm. Note that the amount of demagnification was chosen so as to correspond to the level of the applied axial incremental strain during the *in situ* test.

B.1. Choice of DVC in-plane window size

As detailed in Section 3.2, the presented kinematic fields resulted from a "local" DVC computation on a fine regularly-spaced grid. The thin structure of the textile imposed the choice of a single window along the thickness direction. To select the in-plane window size, a series of local DVC computations between the reference and the "zoomed out" scan was run for a range of contiguous correlation window sizes.

For each orthogonal direction, the evolution of the measured mean strain of all windows is shown in Fig. B.11, along with the corresponding standard deviation (*i.e.*, 1σ). The imposed homogeneous demagnification is also shown in a thick dashed line. The well-known [43,51] trade-off between the spatial resolution of the measurement and the level of the measurement uncertainty is demonstrated. Smaller windows correspond to more measurement points, in the cost of higher uncertainties which can dominate the signal.

Regarding the in-plane deformation, it can be seen that for a window larger than 71×71 px the imposed strain (thick dashed line) is retrieved. Therefore, the size of the in-plane window for the *in situ* test analysis was set to 91×91 px. Any in-plane strain component presented in this work is accompanied by an error defined by the corresponding standard deviation. Conversely, for the out-of-plane direction, a constant discrepancy from the imposed strain in the order of 2% is computed, regardless of the in-plane window size. This is attributed to the highly anisotropic texture of the material, with a considerably weaker gradient at this direction. It should be reminded here that during the *in situ* test a significant amount of dilation was
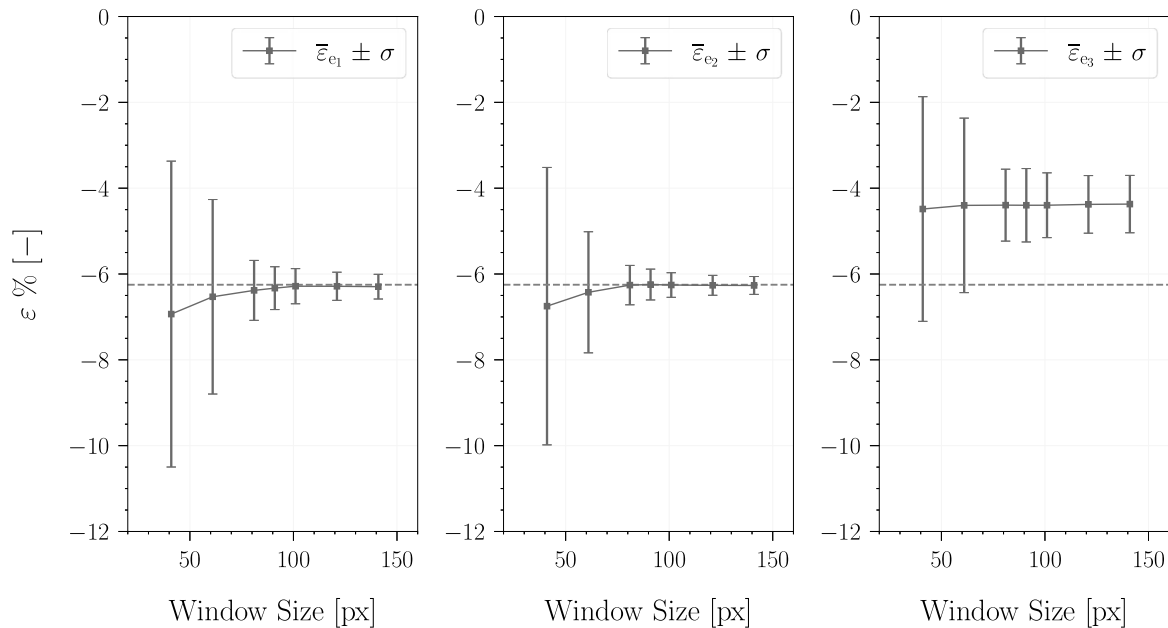

Fig. B.11. Evolution of normal strain components for a range of window sizes for the correlation between the reference and the "zoomed out" scan. Note that the imposed strain is 6.3%.
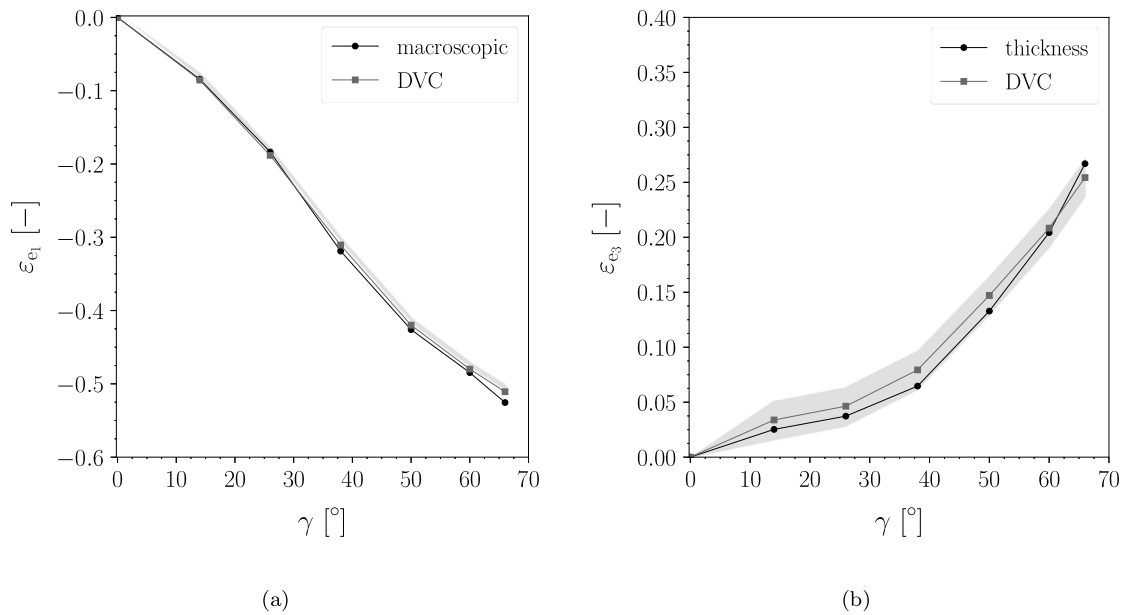
(a)

(b)

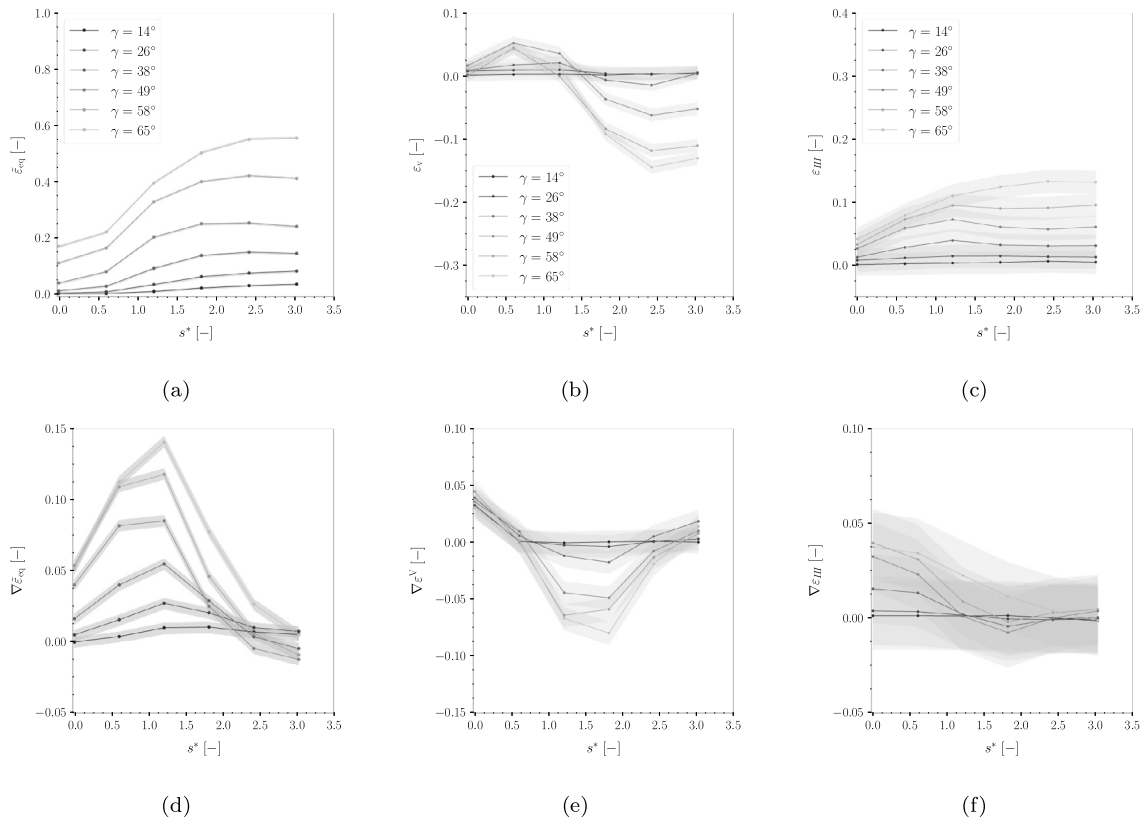**Fig. B.12.** Comparison between macroscopic and DVC measurements for the central region D.

(a)

(b)

(c)

(d)

(e)

(f)

Fig. C.13. Evolution of in-plane equivalent shear strain $\tilde{\varepsilon}_{eq}$ (a), the volumetric strain ε_v (b) and the out-of-plane strain ε_{III} (c) along the adjacent region A–B (the path is sketched in Fig. 1), together with their respective gradients $\nabla_s \tilde{\varepsilon}_{eq}$ (d), $\nabla_s \varepsilon_v$ (e) and $\nabla_s \varepsilon_{III}$ as functions of the dimensionless curvilinear abscissa s^*.

measured along the material direction, reaching 30%. The assessed 2% out-of-plane deformation error is well-quantified and accompanies any corresponding measurement given in this study.

B.2. Cross-validation of DVC strain measurements

To further assess the validity of the kinematic measurements, the in-plane compaction of the tested woven fabric was measured by hand.

More specifically, in the enhanced projection of the reference scan, a zone inside the central region D (see Fig. 1) covering 3 period lengths of the textile was selected. This region was then identified by eye in the remaining enhanced projections and its change of width is plotted in Fig. B.12a. For the same region, the strain evolution along the e_1 direction as measured by DVC is also plotted. It can be seen that the strain values measured by hand are in a very good agreement with the DVC measurements, both indicating a large in-plane compaction of the
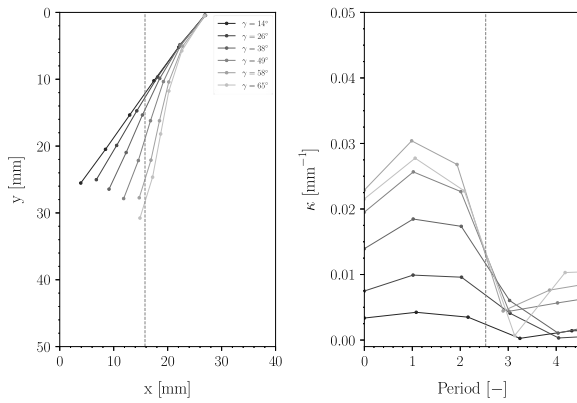
Fig. C.14. Evolution of the yarn centerline along profile line A–B in the fabric plane (left) and its curvature as a function of the dimensionless abscissa (right).

twill fabric. In the same context, Fig. B.12b compares the evolution of the normalized thickness (see Section 3.1) of this region to the measured out-of-plane strain ε_{III} along the material direction (*i.e.*, e_3). Within the measurement uncertainty as quantified through the zoomed out scan, it is shown that the out-of-plane measurements are in a good agreement, both revealing the marked auxetic effect.

Appendix C. Strain and strain gradient profile along line A-B

See Figs. C.13 and C.14.

References

[1] Suemasu H, Friedrich K, Hou M. On deformation of woven fabric-reinforced thermoplastic composites during stamp-forming. Compos Manuf 1994;5(1):31–9.

[2] Cao J, Akkerman R, Boisse P, Chen J, Cheng H, De Graaf E, Gorczyca J, Harrison P, Hivet G, Launay J, et al. Characterization of mechanical behavior of woven fabrics: experimental methods and benchmark results. Composites A 2008;39(6):1037–53.

[3] Zhu B, Yu T, Tao X. Large deformation and slippage mechanism of plain woven composite in bias extension. Composites A 2007;38(8):1821–8.

[4] Boisse P, Hamila N, Guzman-Maldonado E, Madeo A, Hivet G, Dell'Isola F. The bias-extension test for the analysis of in-plane shear properties of textile reinforcements and prepregs: a review. Int J Mater Form 2017;10(4):473–92.

[5] Lebrun G, Bureau MN, Denault J. Evaluation of bias-extension and picture-frame test methods for the measurement of intraply shear properties of PP/glass commingled fabrics. Compos Struct 2003;61(4):341–52.

[6] Harrison P, Clifford MJ, Long A. Shear characterisation of viscous woven textile composites: a comparison between picture frame and bias extension experiments. Compos Sci Technol 2004;64(10–11):1453–65.

[7] Bel S, Boisse P, Dumont F. Analyses of the deformation mechanisms of non-crimp fabric composite reinforcements during preforming. Appl Compos Mater 2012;19(3–4):513–28.

[8] Badel P, Vidal-Sallé E, Maire E, Boisse P. Simulation and tomography analysis of textile composite reinforcement deformation at the mesoscopic scale. Compos Sci Technol 2008;68(12):2433–40.

[9] Latil P, Orgéas L, Geindreau C, Dumont P, Rolland du Roscoat S. Towards the 3D in situ characterisation of deformation micro-mechanisms within a compressed bundle of fibres. Compos Sci Technol 2011;71:480–8.

[10] Charmetant A, Vidal-Sallé E, Boisse P. Hyperelastic modelling for mesoscopic analyses of composite reinforcements. Compos Sci Technol 2011;71(14):1623–31.

[11] Ferretti M, Madeo A, Dell'Isola F, Boisse P. Modeling the onset of shear boundary layers in fibrous composite reinforcements by second-gradient theory. Z Math Phys 2014;65(3):587–612.

[12] Madeo A, Barbagallo G, d'Agostino MV, Boisse P. Continuum and discrete models for unbalanced woven fabrics. Int J Solids Struct 2016;94:263–84.

[13] Barbagallo G, Madeo A, Azehaf I, Giorgio I, Morestin F, Boisse P. Bias extension test on an unbalanced woven composite reinforcement: Experiments and modeling with a second-gradient continuum approach. J Compos Mater 2017;51(2):153–70.

[14] d'Agostino M, Giorgio I, Greco L, Madeo A, Boisse P. Continuum and discrete models for structures including (quasi-) inextensible elasticae with a view to the design and modeling of composite reinforcements. Int J Solids Struct 2015;59:1–17.

[15] Harrison P. Modelling the forming mechanics of engineering fabrics using a mutually constrained pantographic beam and membrane mesh. Composites A 2016;81:145–57.

[16] Lomov SV, Ivanov D, Truong T, Verpoest I, Baudry F, Bosche KV, Xie H. Experimental methodology of study of damage initiation and development in textile composites in uniaxial tensile test. Compos Sci Technol 2008;68(12):2340–9.

[17] Carvelli V, D'Ettorre A, Lomov SV. Acoustic emission and damage mode correlation in textile reinforced PPS composites. Compos Struct 2017;163:399–409.

[18] Wang L, Wu J, Chen C, Zheng C, Li B, Joshi SC, Zhou K. Progressive failure analysis of 2D woven composites at the meso-micro scale. Compos Struct 2017;178:395–405.

[19] Potluri P, Ciurezu DP, Ramgulam R. Measurement of meso-scale shear deformations for modelling textile composites. Composites A 2006;37(2):303–14.

[20] Montesano J, Bougherara H, Fawaz Z. Application of infrared thermography for the characterization of damage in braided carbon fiber reinforced polymer matrix composites. Composites B 2014;60:137–43.

[21] Bruck H, McNeill S, Sutton MA, Peters W. Digital image correlation using Newton-Raphson method of partial differential correction. Exp Mech 1989;29(3):261–7.

[22] Lomov SV, Boisse P, Deluycker E, Morestin F, Vanclooster K, Vandepitte D, Verpoest I, Willems A. Full-field strain measurements in textile deformability studies. Composites A 2008;39(8):1232–44.

[23] Willems A, Lomov SV, Verpoest I, Vandepitte D. Optical strain fields in shear and tensile testing of textile reinforcements. Compos Sci Technol 2008;68(3–4):807–19.

[24] Carvelli V, Pazmino J, Lomov SV, Verpoest I. Deformability of a non-crimp 3D orthogonal weave E-glass composite reinforcement. Compos Sci Technol 2012;73:9–18.

[25] Zhao X, Liu G, Gong M, Song J, Zhao Y, Du S. Effect of tackification on in-plane shear behaviours of biaxial woven fabrics in bias extension test: Experiments and finite element modeling. Compos Sci Technol 2018;159:33–41.

[26] Maire E, Withers P. Quantitative X-ray tomography. Int Mater Review 2014;59:1–43.

[27] Garcea S, Wang Y, Withers P. X-ray computed tomography of polymer composites. Compos Sci Technol 2018;156:305–19.

[28] Naouar N, Vasiukov D, Park C, Lomov S, Boisse P. Meso-FE modelling of textile composites and X-ray tomography. J Mater Sci 2020;55(36):16969–89.

[29] Abdul Ghafour T, Balbinot C, Audry N, Martoïa F, Orgéas L, Dumont P, Vroman E, Boller E. Permeability of flax fibre mats: numerical and theoretical prediction from 3D X-ray microtomography images. Composites A 2021;151:106644.

[30] Syerko, et al. Benchmark exercise on image-based permeability determination of engineering textiles: Microscale predictions. Composites A 2023;167:107397.

[31] Schilling PJ, Karedla BR, Tatiparthi AK, Verges MA, Herrington PD. X-ray computed microtomography of internal damage in fiber reinforced polymer matrix composites. Compos Sci Technol 2005;65(14):2071–8.

[32] Croom B, Wang W-M, Li J, Li X. Unveiling 3D deformations in polymer composites by coupled micro X-ray computed tomography and volumetric digital image correlation. Exp Mech 2016;56(6):999–1016.

[33] Chateau C, Gélébart L, Bornert M, Crépin J, Boller E, Sauder C, Ludwig W. In situ X-ray microtomography characterization of damage in SiCf/SiC minicomposites. Compos Sci Technol 2011;71(6):916–24.

[34] Li Z, Guo L, Zhang L, Wang Q. In situ experimental investigation on the out-plane damage evolution of 3D woven carbon-fiber reinforced composites. Compos Sci Technol 2018;162:101–9.

[35] Ferré Sentis D, Cochereau T, Orgéas L, Dumont P, Rolland du Roscoat S, Laurencin T, Terrien M, Sager M. Tensile behaviour of uncured sheet moulding compounds: Rheology and flow-induced microstructures. Composites A 2017;101:459–70.

[36] Ferré Sentis D, Orgéas L, Dumont P, Rolland du Roscoat S, Sager M, P. L. 3D in situ observations of the compressibility and pore transport in sheet moulding compounds during the early stages of compression moulding. Composites A 2017;92:51–61.

[37] Laurencin T, Dumont P, Orgéas L, Le Corre S, Martoïa F, Rolland du Roscoat S, Laure P. 3D real time and in situ observation of the fibre orientation during the plane strain flow of concentrated fibre suspensions. J Non-Newt Fluid Mech 2023;312:104978.

[38] Mazars V, Caty O, Couégnat G, Bouterf A, Roux S, Denneulin S, Pailhès J, Vignoles GL. Damage investigation and modeling of 3D woven ceramic matrix composites from X-ray tomography in-situ tensile tests. Acta Mater 2017;140:130–9.

[39] Mendoza A, Schneider J, Parra E, Roux S. The correlation framework: Bridging the gap between modeling and analysis for 3D woven composites. Compos Struct 2019;229:111468.

[40] Schindelin J, Arganda-Carreras I, Frise E, et al. Fiji an open source platform for biological image analysis. Nature Methods 2012;9:676–82.

[41] Rezakhaniha R, Agianniotis A, Schrauwen JTC, Griffa A, Sage D, Bouten Cv, Van De Vosse F, Unser M, Stergiopulos N. Experimental investigation of collagen waviness and orientation in the arterial adventitia using confocal laser scanning microscopy. Biomech Model Mechanobiol 2012;11(3):461–73.

[42] Bay BK, Smith TS, Fyhrie DP, Saad M. Digital volume correlation: three-dimensional strain mapping using X-ray tomography. Exp Mech 1999;39(3):217–26.

[43] Hild F, Roux S. Comparison of local and global approaches to digital image correlation. Exp Mech 2012;52(9):1503–19.

[44] Lhuissier P, Bormann T, Pelloux G, Bataillon X, Pelloux F, Josserond C, Gravier P, Blandin J-J, Boller E, Salvo L. High-temperature deformation followed in situ by X-ray microtomography: a methodology to track features under large strain. J Synchrotron Rad 2021;28(2).

[45] Harris CG, Stephens M, et al. A combined corner and edge detector. In: Alvey vision conference, Vol. 15. Citeseer; 1988, p. 10–5244.

[46] Doumalin P. Microextensométrie locale par corrélation d'images numériques. Application aux études micromécaniques par microscopie électronique à balayage. (Ph.D. thesis), Ecole Polytechnique X; 2000.

[47] Stamati E, Roubin E, R. C, et al. SPAM: Software for practical analysis of materials. J Open Source Soft 2020;5(50):2286.

[48] Stamati O. Impact of meso-scale heterogeneities on the mechanical behaviour of concrete: insights from in-situ x-ray tomography and E-FEM modelling (Thesis), Université Grenoble Alpes ; 2020.

[49] Tudisco E, Jailin C, Mendoza A, Tengattini A, Andò E, Hall SA, Viggiani G, Hild F, Roux S. An extension of digital volume correlation for multimodality image registration. Meas Sci Technol 2017;28(9):095401.

[50] Lucas BD, Kanade T, et al. An iterative image registration technique with an application to stereo vision. 1981.

[51] Grédiac M, Hild F. Full-field measurements and identification in solid mechanics. Wiley Online Library; 2013.

[52] Robitaille F, Gauvin R. Compaction of textile reinforcements for composites manufacturing. I: Review of experimental results. Polym Compos 1998;19:198–216.

[53] Ahmad Z, Sirková BK. Tensile behavior of Basalt/Glass single and multilayer-woven fabrics. J Text Inst 2018;109(5):686–94.

[54] Bowen R. Theory of mixtures - volume 3 of continuum physics, , mixtures and em field theories. Cambridge: Academic Press; 1976.

[55] Charmetant A, Orliac JG, Vidal-Sallé E, Boisse P. Hyperelastic model for large deformation analyses of 3D interlock composite preforms. Compos Sci Technol 2012;72(12):1352–60.

[56] Nasri M, Garnier C, Abbassi F, Labanieh AR, Dalverny O, Zghal A. Hybrid approach for woven fabric modelling based on discrete hypoelastic behaviour and experimental validation. Compos Struct 2019;209:992–1004.

[57] Verma P, Shofner M, A.C. G. Deconstructing the auxetic behavior of paper. Basic Solid State Phys 2014;251:289–96.

[58] Rodney D, Gadot B, Riu Martinez O, Rolland du Roscoat S, Orgéas L. Reversible dilatancy in entangled singlewire materials. Nat Mater 2016;15:72–6.

[59] Shukla S, Behera B. Auxetic fibrous structures and their composites: A review. Compos Struct 2022;290:115530.

[60] Launay J, Hivet G, Duong A, Boisse P. Experimental analysis of the influence of tensions on in plane shear behaviour of woven composite reinforcements. Compos Sci Technol 2008;68:506–15.

[61] Desrues J, Andò E. Strain localisation in granular media. C R Phys 2015;16(1):26–36.

[62] Barbagallo G, Madeo A, Morestin F, Boisse P. Modelling the deep drawing of a 3D woven fabric with a second gradient model. Math Mech Solids 2017;22(11):2165–79.

[63] Boisse P, Colmars J, Hamila N, Naouar N, Steer Q. Bending and wrinkling of composite fiber preforms and prepregs. A review and new developments in the draping simulations. Composites B 2018;141:234–49.